ACS OMEGA

http://pubs.acs.org/journal/acsodf

Article

New Dication-Based Lead-Deficient 3D $MAPbI_3$ and $FAPbI_3$ "d-HPs" Perovskites with Enhanced Stability

Liam Gollino, Antonin Leblanc, Jens Dittmer, Nicolas Mercier,* and Thierry Pauporté*

Cite This: *ACS Omega* 2023, 8, 23870−23879

Read Online

ACCESS | Metrics & More | Article Recommendations | Supporting Information

ABSTRACT: Toxicity induced by the presence of lead and the rather poor stability of halide perovskite semiconductors represent the major issues for their large-scale application. We previously reported a new family of lead- and iodide-deficient $MAPbI_3$ and $FAPbI_3$ perovskites called d-HPs (for lead- and iodide-deficient halide perovskites) based on two organic cations: hydroxyethylammonium $HO-(CH_2)_2-NH_3^+$ (HEA^+) and thioethylammonium $HS-(CH_2)_2-NH_3^+$ (TEA^+). In this article, we report the use of an organic dication, 2-hydroxypropane-1,3-diaminium (2-propanol 1,3 diammonium), named PDA^{2+}, to create new 3D d-HPs based on the $MAPbI_3$ and $FAPbI_3$ network with general formulations of $(PDA)_{0,88x}(MA)_{1-0,76x}[Pb_{1-x}I_{3-x}]$ and $(PDA)_{1,11x}(FA)_{1-1,22x}[Pb_{1-x}I_{3-x}]$, respectively. These d-HPs have been successfully synthesized as crystals, powders, and thin films and exhibit improved air stability compared to their reference $MAPbI_3$ and $FAPbI_3$ perovskite counterparts. PDA^{2+}-based deficient $MAPbI_3$ was also tested in operational perovskite solar cells and exhibited an efficiency of 13.0% with enhanced stability.

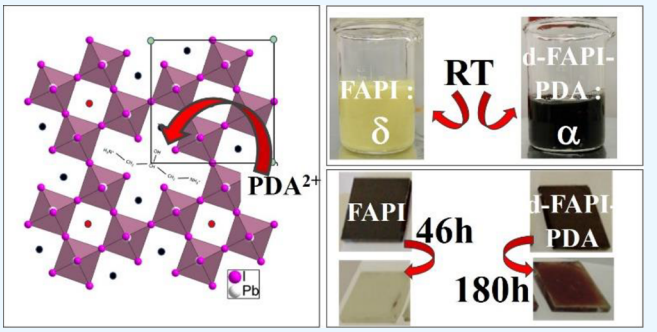

INTRODUCTION

Hybrid halide perovskites are promising semiconductors with numerous interesting optoelectronic properties.[1−9] They have been studied for various applications such as lasers,[10] LEDs,[11] photodetectors,[12,13] scintillation[14] and solar cells (PSCs).[15−23] Unfortunately, the main drawback of the current perovskite materials is their rather poor stability[15−17] and their toxicity caused by the presence of lead.[18−23] This severely hinders their commercialization and calls for the finding of new perovskite systems.

One of the solutions to resolve this issue is to totally[24−27] or partially replace lead by another element.[28] However, substituting lead by another element remains uneasy and is a major concern as it faces important limitations. The substitution element has to be a metal ion that can form a 3D perovskite structure. To be stable, halide as well as oxide perovskites then need to respect tolerance factors. The 3D perovskite structure and stability are governed by the Goldschmidt tolerance factor,[29] which was subsequently updated by Bartel et al.[30] As a reminder, hybrid halide perovskite has the ABX_3 general formula, where A is a monovalent organic or inorganic cation (mainly Cs^+, $CH_3NH_3^+$ (methylammonium noted MA^+), or $HC(NH_2)_2^+$ (formamidinium noted FA^+), B is an octahedrally coordinated divalent metal ion (classically Pb^{2+}), and X is a halogen (generally Cl^-, Br^-, or I^-).[15,31−33]

In the last years, we have reported a new family of 3D perovskites called d-HPs for "lead- and iodide-deficient halide perovskites" which retains the 3D structure but with PbI^+ deficiencies caused by the insertion of large organic cations and circumventing the tolerance factor. Up to this day, two d-HPs have been developed based on the insertion of hydroxyethylammonium (HEA^+)[34,35] and thioethylammonium (TEA^+)[35] cations. Another group developed similar perovskites with lead deficiencies caused by the insertion of ethylenediammonium cations, and they are called "Hollow" perovskites.[36−43]

This work extends the d-HP family by the employment of a dication with six non-hydrogen atoms. When a large A′ diammonium cation is added to prepare halide perovskites, a multilayered 2D Dion-Jacobson $A'(A)_{n-1}Pb_nI_{3n+1}$ phase is expected to be formed.[44−47] However, in the presently explored MAI/PDA^{2+} and FAI/PDA^{2+} systems, where 2-hydroxypropane-1,3-diaminium (2-propanol 1,3 diammonium) is $^+NH_3CH_2CH(OH)CH_2NH_3^+$, noted PDA^{2+}, a different crystal phase which retains a 3D structure has been formed despite the use of such a diammonium cation. We synthesized $MAPbI_3$ (MAPI) and $FAPbI_3$ (FAPI) perovskites with the same PDA^{2+} dication inserted within the lattice that we named *d*-MAPI-PDA_x and *d*-FAPI-PDA_x, respectively. We show that they form a 3D d-HP structure. A similar phenomenon had

Received: April 5, 2023
Accepted: May 16, 2023
Published: June 23, 2023

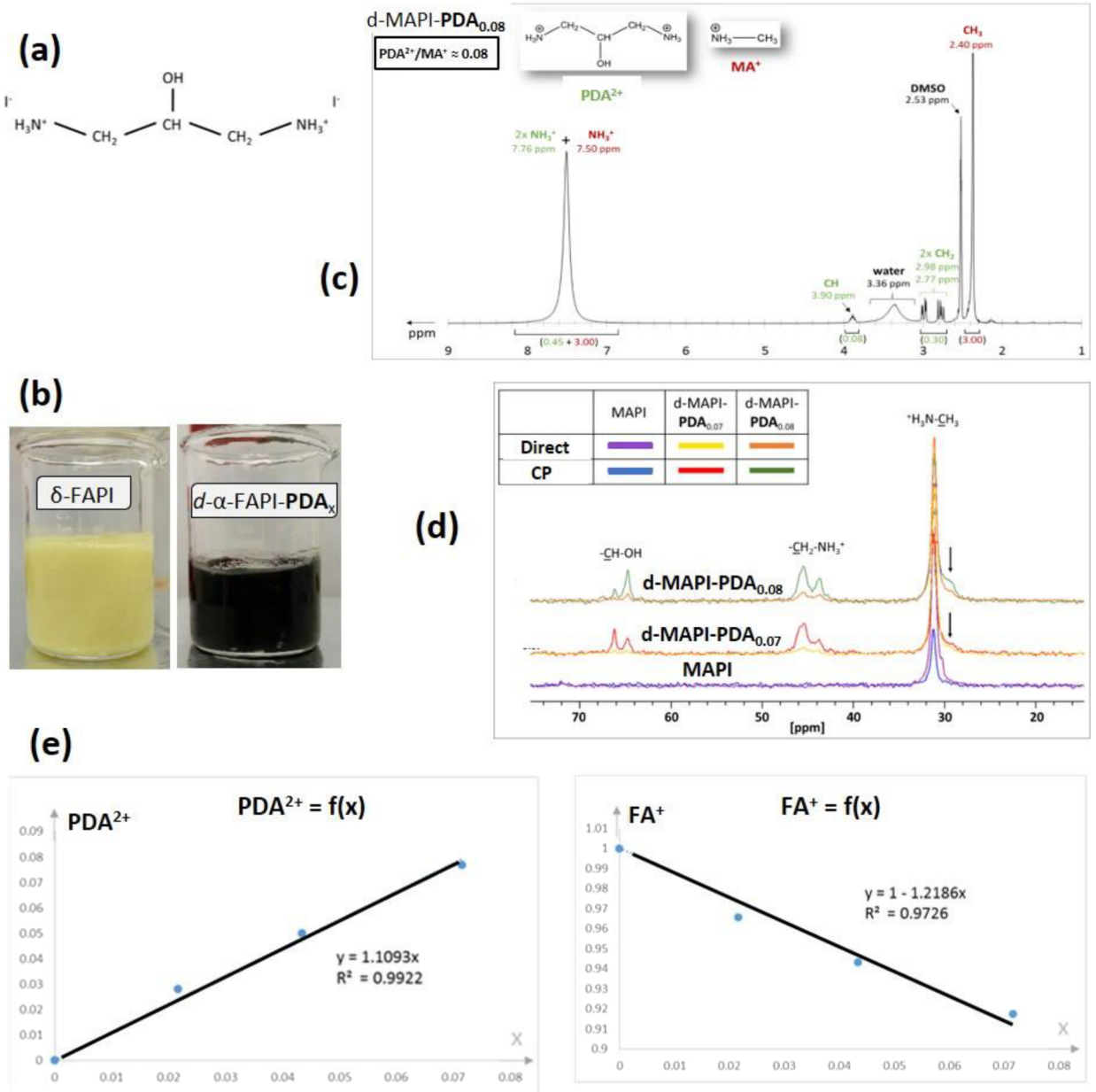

Figure 1. (a) PDA^{2+} cation (with I^- counterions represented). (b) Room temperature synthesis of δ-FAPI (yellow) and *d*-α-FAPI-PDA_x (black), a lead and iodide deficient 3D halide perovskite containing PDA^{2+} dication. (c) ^1H NMR of *d*-MAPI-$PDA_{0.08}$ crystallized powder solubilized in *DMSO*-d_6 (d) ^{13}C direct excitation and cross-polarization (CP) solid-state NMR of *d*-MAPI-PDA_x crystallized powders and $MAPbI_3$. (e) Linear relationships of PDA^{2+} and FA^+ contents with x (x = number of lead and iodide vacancies), leading to the proposed formulation of $(PDA)_{1,11x}(FA)_{1-1,22x}[Pb_{1-x}I_{3-x}]$ for *d*-α-FAPI-PDA compounds.

been already reported for "Hollow" perovskite with ethylenediammonium[36−42] and two long dications, namely, propylenediammonium and trimethylenediammonium[43] based on five non-hydrogen atoms. However, the PDA^{2+} dication contains additionally an alcohol function. The general formulations of *d*-MAPI-PDA_x and *d*-FAPI-PDA_x are established as $(PDA)_{0,88x}(MA)_{1-0,76x}[Pb_{1-x}I_{3-x}]$ and $(PDA)_{1,11x}(FA)_{1-1,22x}[Pb_{1-x}I_{3-x}]$, respectively. These perovskites have been synthesized as single crystals for *d*-MAPI-PDA_x, as powders and thin films for *d*-MAPI-PDA_x and *d*-FAPI-PDA_x. They have been fully characterized to assess the correct incorporation of PDA^{2+} in the lattice, as well as the formation of the d-HP structure. Tuning of the perovskites optoelectronic properties has been determined by varying the amount of PDA^{2+} inserted in the crystal structure. Astonishing air stability has also been found. Finally, we show the first results on the use of *d*-MAPI-PDA in perovskite solar cells.

RESULTS AND DISCUSSION

In a system consisting of PbI_2, MAI, or FAI and a suitable organic dication $A'I_2$ (A'^{2+} being a dication with two primary ammonium functional groups), multilayered 2D Dion-Jacobson halide perovskites, $A'(MA)_{n-1}Pb_nI_{3n+1}$, are expected to form.[44−47] However, insertion of the PDA^{2+} dication, whose molecular structure is displayed in Figure 1a, led to a different behavior. This cation was selected because a part of its skeleton "$^+NH_3-CH_2-CH(OH)-$" is comparable to the HEA^+ cation whose ability to produce a d-HP structure has been

https://doi.org/10.1021/acsomega.3c02292
ACS Omega 2023, 8, 23870−23879

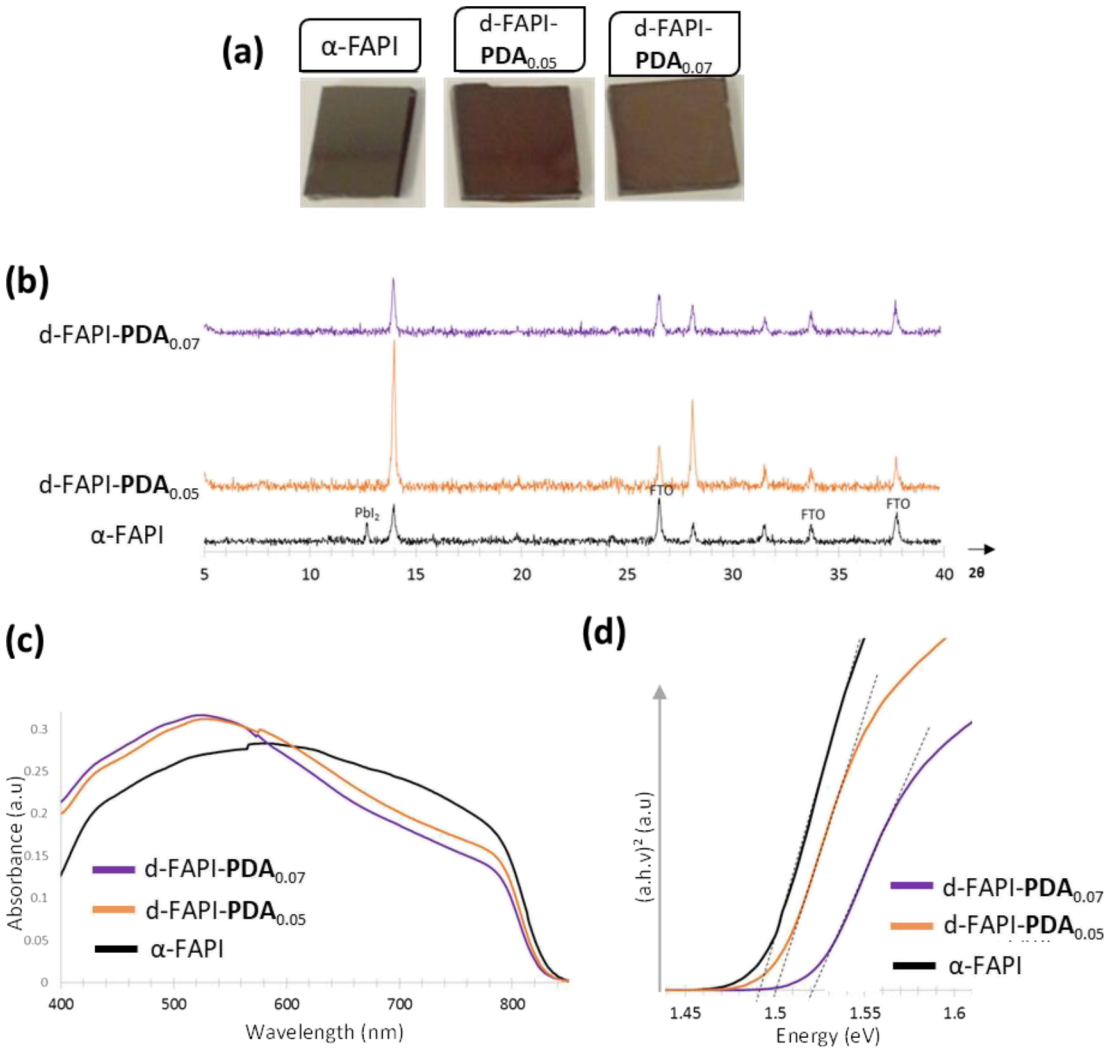

Figure 2. Characterizations of FAPI, *d*-FAPI-PDA$_{0.05}$, and *d*-FAPI-PDA$_{0.07}$ films. (a) Films images; (b) XRD patterns. (c) UV−visible absorbance spectra and (d) absorption edge Tauc plots.

demonstrated previously (Figure S1).[34,35] Our first tests of single crystals growths using the liquid−gas diffusion method or inverse temperature crystallization method did not lead to a Dion−Jacobson (DJ) phase, but, systematically, to homogeneous samples of black crystals (Figure S2, Supporting Information). Single crystal X-ray diffraction showed a unit cell corresponding to the 3D $MAPbI_3$ perovskite. However, the ^1H nuclear magnetic resonance (NMR) spectra of well-washed and dried black crystals solubilized in deuterated dimethylsulfoxyde (*DMSO-d*$_6$) revealed the presence of both MA^+ and PDA^{2+} cations (Figure S6a, Supporting Information − case of $PDA^{2+}/MA^+ = 0.03$) meaning that a small quantity of PDA^{2+} dications was incorporated into the 3D framework. The PDA^{2+} dication contains six non-hydrogen atoms, and the retaining of a 3D structure instead of the formation of a 2D DJ upon incorporation of such long chain is a first to our knowledge.

The corresponding *d*-MAPI-PDA$_x$ compounds as well as *d*-*α*-FAPI-PDA$_x$ compounds (x = number of vacancies in lead- and iodide-deficient $Pb_{1-x}I_{3-x}$ network) have been prepared as crystallized powders at room temperature through precipitation when a *γ*-butyrolactone (GBL) solution containing PbI_2, MAI, or FAI and $PDAI_2$ reagents was poured into an ethyl acetate solution. It is worth noting that while, as well-known, the yellow powder of *δ*-FAPI precipitates at room temperature from PbI_2 and FAI, a black powder was systematically obtained when $PDAI_2$ was added to the system at room temperature (Figure 1b). This is a good indication that the black powder is not *α*-FAPI but *d*-*α*-FAPI-PDA$_x$, which is the 3D halide perovskite with lead and iodide vacancies and incorporating the PDA^{2+} dication. Using this approach, we have obtained and fully characterized several compounds: *d*-MAPI-PDA$_{0.05}$, *d*-MAPI-PDA$_{0.07}$, *d*-MAPI-PDA$_{0.08}$, *d*-*α*-FAPI-PDA$_{0.02}$, *d*-*α*-FAPI-PDA$_{0.04}$, *d*-*α*-FAPI-PDA$_{0.07}$ (details in the SI, see photograph in Figure S3, Supporting Information). Powder X-ray diffraction (PXRD) patterns of these samples are comparable to the one of MAPI and *α*-FAPI, (Figures S4 and S5, Supporting Information). Energy dispersive X-ray (EDX) measurements were carried out on powders of MAPI and *α*-FAPI references compounds as well as on PDA^{2+}-based samples that revealed a I/Pb ratio superior to 3 (3.11−3.17 range and 3.04−3.15 range for the *d*-MAPI-PDA$_x$ and *d*-FAPI-PDA$_x$ series, respectively) as found in lead- and iodide-deficient $Pb_{1-x}I_{3-x}$ networks (Table S1, Supporting Information). Assuming the same kind of inorganic networks, x values are in the 0.05−0.08 and 0.02−0.07 ranges for the *d*-MAPI-PDA$_x$ and *d*-FAPI-PDA$_x$ series, respectively, which were deducted from EDX results. The PDA^{2+}/MA^+ and

https://doi.org/10.1021/acsomega.3c02292
ACS Omega 2023, 8, 23870−23879

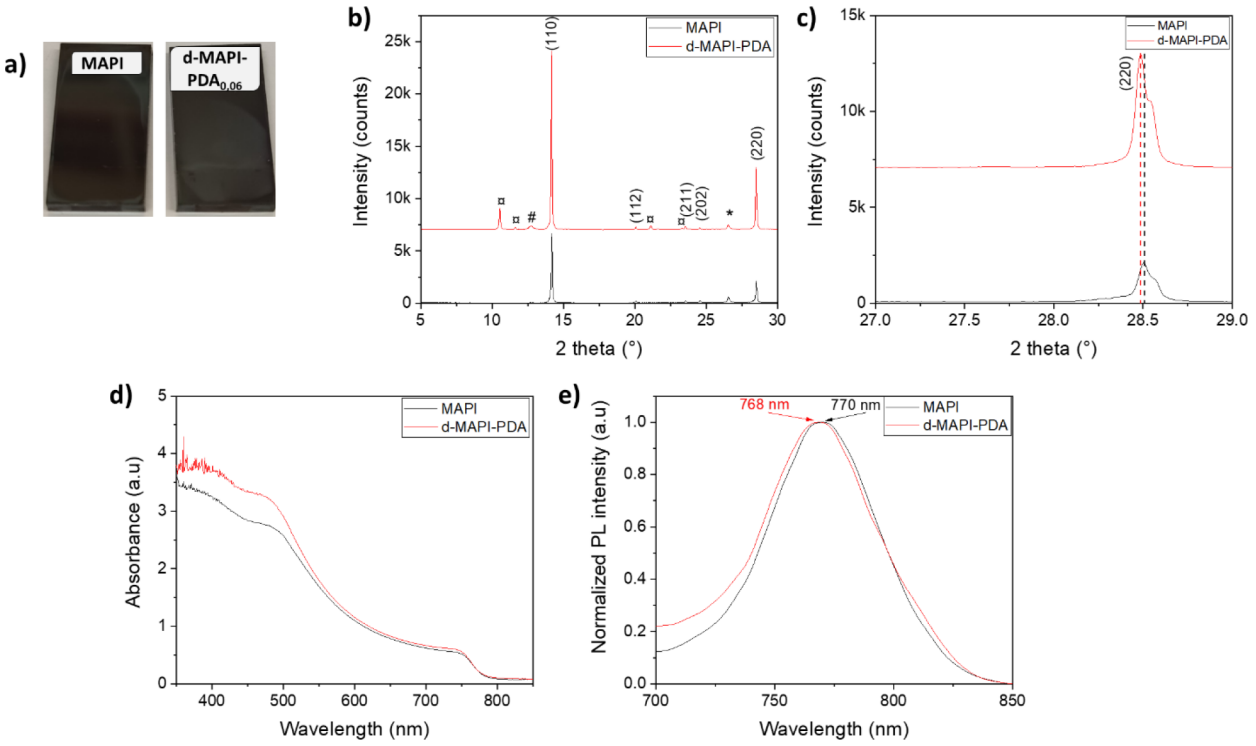

Figure 3. Characterizations of MAPI and *d*-MAPI-PDA films. (a) Pictures of films. (b) XRD patterns of MAPI and *d*-MAPI-PDA films. (c) Same as (b) zoomed between 27 and 29°. (d) UV−visible absorbance. (e) Steady-state PL spectra of MAPI and *d*-MAPI-PDA films.

PDA^{2+}/FA^+ ratios were determined from ^1H NMR of *DMSO-*d_6 solutions in which crystallized powders were solubilized (Figures S7 and S8, Supporting Information). Figure 1c gives an example of the presence of signals of both cations. The peak integration gave a PDA^{2+}/MA ratio of 0.08 for this sample. ^{13}C solid-state NMR experiments confirmed the insertion of PDA^{2+} into the lattice. The spectrum of *d*-MAPI-$PDA_{0.08}$ is given in Figure 1d. As expected, it shows one ^{13}C signal at 31 ppm corresponding to the $-\underline{C}H_3$ group of the MA^+ cation, while two ^{13}C double signals at 45 and 65 ppm are associated to the $-\underline{C}H_2-NH_3^+$ and $-\underline{C}H-OH$ groups of the PDA^{2+} cation, respectively. A low intensity shoulder at 29 ppm was noticed, indicating that MA^+ cations occupy another site with a different environment. With regard to the PDA^{2+} signal, we first notice that they do not correspond to the ones of $PDAI_2$ (Figure S9), meaning that the organic iodide salt is not present on the crystal surface or grain boundaries. Similar to MA^+, both types of carbon atoms of PDA^{2+} show a distribution of sites with two maxima, here also indicating two main types or environments. These observations agree with the existence of a deficient $[Pb_{1-x}I_{3-x}]$ network which offers several potential sites for organic cation insertion. Direct excitation spectra, although showing only very weak PDA^{2+} signals, confirm that the cross-polarization (CP) signals are representative. The big PDA^{2+} cation is relatively immobile in terms of molecular reorientation so that the CP experiments are more efficient. The CP intensity of the small MA^+ ions is also enhanced in both *d*-MAPI-PDA_x compared to MAPI, showing that the motions of MA^+ are also more constrained in this structure. With regard to (i) the $Pb_{1-x}I_{3-x}$ network bearing a negative charge of $(1 + x)$ that must be counterbalanced by a positive charge of $(1 + x)$ borne by organic cations and (ii) the PDA^{2+}/MA^+ or PDA^{2+}/FA^+ ratio obtained from ^1H NMR experiments, a formulation for each *d*-MAPI-PDA_x and *d*-FAPI-PDA_x sample was found (Tables S2 and S3, Supporting Information). Plotting $PDA^{2+} = f(x)$ and MA^+ or $FA^+ = f(x)$ reveals linear relationships (Figure 1e for *d*-*α*-FAPI-PDA_x and Figure S10, Supporting Information, for *d*-MAPI-PDA_x). The general formulations of $(PDA)_{0,88x}(MA)_{1-0,76x}[Pb_{1-x}I_{3-x}]$ for *d*-MAPI-PDA_x and $(PDA)_{1,11x}(FA)_{1-1,22x}[Pb_{1-x}I_{3-x}]$ for *d*-*α*-FAPI-PDA_x can thus be proposed. Finally, the C, H, N, O and Pb elemental analyses (Table S4, Supporting Information) are in very good agreement with the sample formulations, validating the general formula of these two series of deficient 3D halide perovskites.

Thin films of *d*-MAPI-PDA_x and *d*-FAPI-PDA_x compounds were then prepared from precursor solutions by spin coating. By varying the stoichiometry of the precursors, two distinct compositions (x values) for each perovskite could be obtained: *d*-MAPI-$PDA_{0.06}$, *d*-MAPI-$PDA_{0.08}$, *d*-FAPI-$PDA_{0.05}$, and *d*-FAPI-$PDA_{0.07}$ for precursor stoichiometry of 1/3/3, 1.25/3/3, 0.75/3/3, and 1/3/3 of $PDAI_2/MAI/PbI_2$ and $PDAI_2/FAI/PbI_2$. The x values of these films were deducted from I/Pb ratios measured by EDX (Table S5, Supporting Information). A $FAPbI_3$ reference film was prepared using the same protocol as *d*-FAPI-PDA_x, except that this film was annealed at 155 °C (while *d*-FAPI-PDA_x films were annealed only at 125 °C). Pictures of the films are shown in Figure 2a. XRD measurements were conducted on *d*-FAPI-PDA_x and FAPI films (Figure 2b). The former display an increase of intensity along the (001) and (002) peaks compared to FAPI, synonym of better crystallinity of the films. The absence of PbI_2 peaks and yellow photoinactive *δ*-FAPI peaks is also noted, and the purity of the *d*-FAPI-PDA_x films is assessed despite the low annealing temperature of 125 °C employed. However, to the exception of the two points aforementioned, *d*-FAPI-PDA_x and FAPI diffractograms coincide perfectly and no shift of the Bragg reflections to smaller angles can be observed. UV−

https://doi.org/10.1021/acsomega.3c02292
ACS Omega 2023, 8, 23870−23879

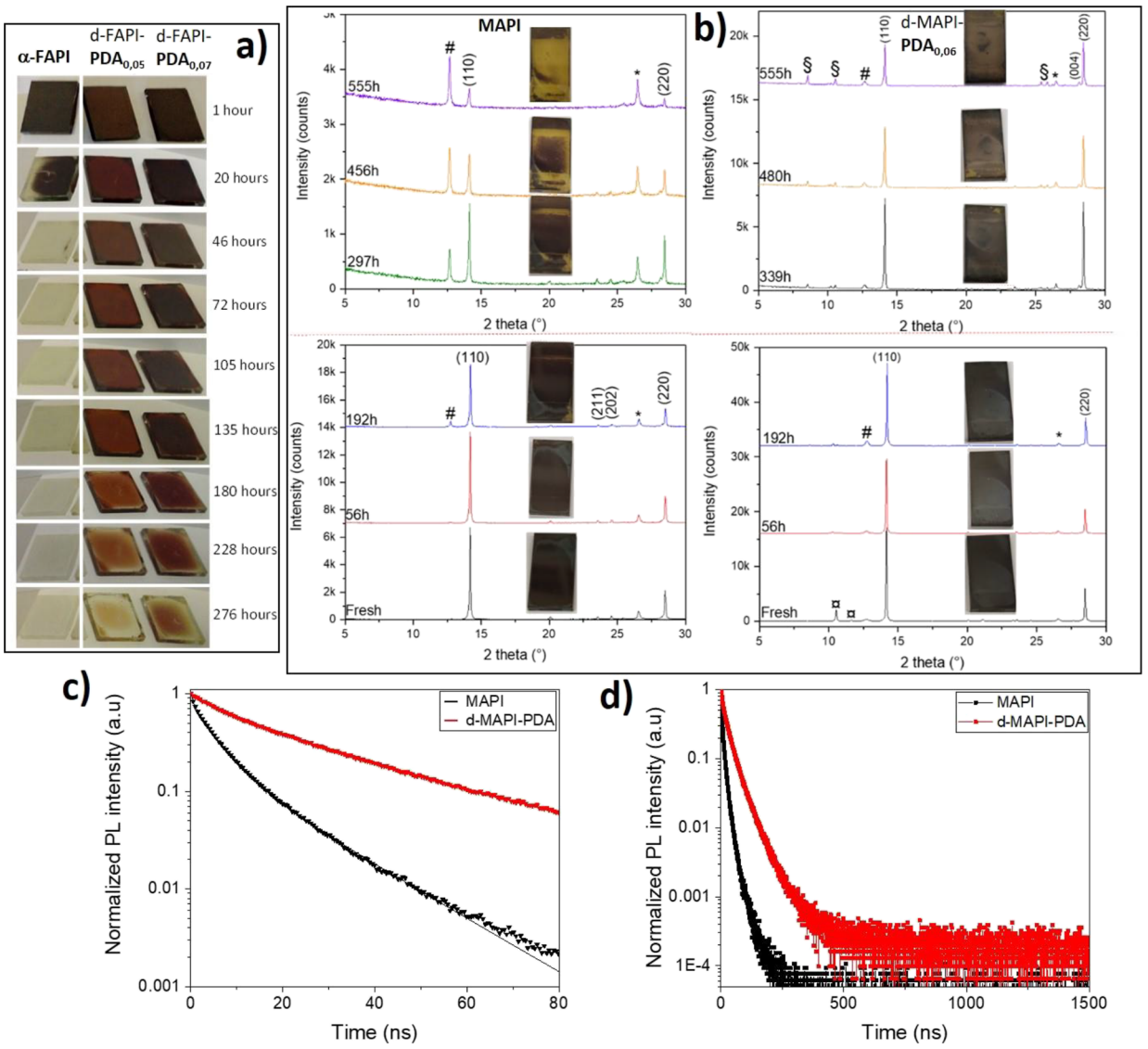

Figure 4. (a) Images of thin films of α-FAPI and d-FAPI-PDA$_x$ (x = 0.05, 0.07) during the aging process (65−80% RH, T° = 20−21 °C). (b) XRD patterns upon the stability test (70−90% RH, T° = 16−18 °C) and corresponding images of thin films of MAPI (left) and d-MAPI-PDA (right). FTO peaks are indicated by the * symbol. # indicates the PbI_2 phase. ¤ indicates the unknown phase present in the fresh d-MAPI-PDA film. § indicates the unknown phase appearing during aging. (c) Normalized time-resolved photoluminescence of MAPI (black trace) and d-MAPI-PDA (red trace) films on FTO/c-TiO_2 substrates measured up to 80 ns. The full lines are the fit curves. (d) Same as (c) measured up to 1500 ns.

visible absorbance measurements were also conducted on d-FAPI-PDA$_x$ and FAPI films (Figure 2c), and they also revealed an increase and a decrease of the absorbance for d-FAPI-PDA$_x$ compared to FAPI between 400−600 and 600−850 nm, respectively. A blue-shift of the absorption edge is observed after PDA^{2+} incorporation within the FAPI lattice. An evolution of the band gap values from 1.49 eV (α-FAPI) to 1.50 eV (d-FAPI-PDA$_{0.05}$) and 1.52 eV (d-FAPI-PDA$_{0.07}$) is also observed by plotting the associated Tauc plots (Figure 2d). These observations confirm the incorporation of PDA^{2+} cations within the FAPI perovskite lattice and thus the lead and iodide deficiency of the $[Pb_{1-x}I_{3-x}]$ inorganic network.

Regarding d-MAPI-PDA$_x$ films, only the d-MAPI-PDA$_{0.06}$ composition was further analyzed. This composition will be named d-MAPI-PDA in the following. Pictures of d-MAPI-PDA and reference MAPI films are shown in Figure 3a. XRD characterization was done to assess the phase and purity of the final d-MAPI-PDA perovskite layer and to compare it to reference MAPI (Figure 3b,c). d-MAPI-PDA displays an impressive increase of intensity along the (110) and (220) peaks compared to MAPI. It proves better crystallinity and high texturing of the film caused by PDA^{2+} insertion into the lattice. We also noticed the presence of the PbI_2 peak at 12.6° for d-MAPI-PDA, which is consistent with the flakes observed on SEM images (Figure S11, Supporting Information). Two new peaks are also present at 10.5 and 11.6° (with their associated harmonics at 21.0 and 23.2°, respectively). We conjecture the presence of PDA^{2+}-related compounds/phases in the perovskite film. A hypothesis is the presence of one or several PDA^{2+}-based layered compounds. However, there is no signature of such phases in the UV−visible absorbance spectra depicted in Figures 3d and S12a. d-MAPI-PDA film also exhibits a small shift of the Bragg reflections to smaller 2θ angles, which indicates an expansion of the unit cell and thus the good insertion of PDA^{2+} into the lattice. It proves the correct synthesis and formation of the d-HP d-MAPI-PDA

https://doi.org/10.1021/acsomega.3c02292
ACS Omega 2023, 8, 23870−23879

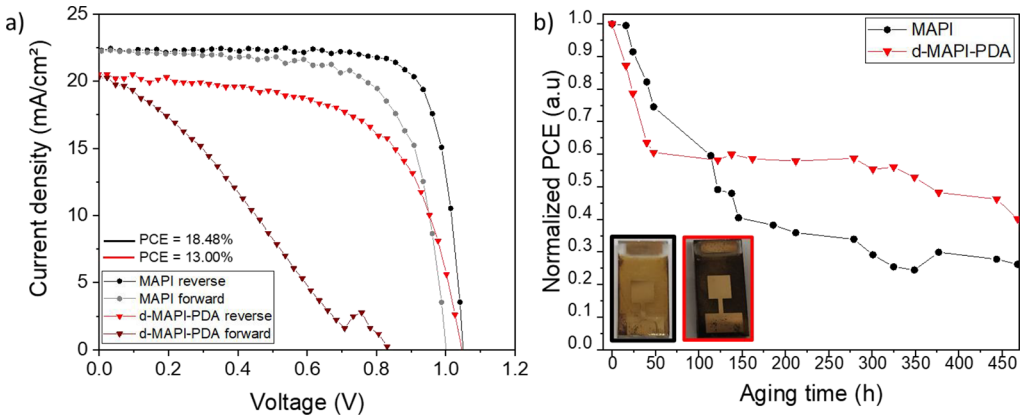

Figure 5. (a) *J*−*V* curves of best MAPI and *d*-MAPI-PDA devices. (b) Normalized PCE evolution of unencapsulated MAPI and *d*-MAPI-PDA devices efficiency as a function of aging time. Storage was made under ambient conditions (70−90% RH, $T°$ = 16−18 °C) and ambient light. Inset: Pictures of MAPI (black frame) and *d*-MAPI-PDA (red frame) devices after 450 h of aging.

perovskite. Figure 3d compares the absorbance spectra of MAPI and *d*-MAPI-PDA films. *d*-MAPI-PDA has higher light absorption throughout the whole near UV−visible region. This better absorbance could be linked to a thicker layer for *d*-MAPI-PDA. The absorption edge is slightly blue-shifted after PDA^{2+} incorporation. Tauc plots of the absorbance spectra (Figure S12b, Supporting Information) show a shift of the optical band gap of 10 meV (1.594 eV for MAPI and 1.604 eV for *d*-MAPI-PDA), in agreement with an expansion of the volume cell unit after PDA^{2+} addition. This is also observed by steady-state PL measurements (Figure 3e), where a slight blue-shift of 2 nm is observed.

We examined the stability of the *d*-FAPI-PDA_x and *d*-MAPI-PDA films by following their XRD patterns and visual aspects after storage in ambient air conditions. Storage conditions of *d*-FAPI-PDA_x films were the relative humidity (RH) = 65−80% and $T°$ = 20−21 °C while *d*-MAPI-PDA conditions were RH = 70−90% and $T°$ = 16−18 °C. By looking at films shown in Figure 4a, we can see fast degradation of $FAPbI_3$ after only 20 h of aging and that the film is completely transparent after 46 h. On the other hand, *d*-FAPI-$PDA_{0.05}$ and *d*-FAPI-$PDA_{0.07}$ films show a slight visible degradation only after 180 h. The diffractograms obtained during film aging confirm what was observed by the eye (Figure S13, Supporting Information). After 20 h, α-FAPI degradation into yellow inactive δ-FAPI started and was completed after 46 h. For *d*-FAPI-PDA_x films, the degradation into the δ-phase started after 180 and 72 h for *d*-FAPI-$PDA_{0.05}$ and *d*-FAPI-$PDA_{0.07}$, respectively. A new peak at 10.5° also appeared for *d*-FAPI-$PDA_{0.07}$ film, which indicates the presence of a new phase, which is unknown to us. This proves that the insertion of PDA^{2+} cations within the $FAPbI_3$ lattice improves the stability of the resulting perovskite.

Figure 4b shows the XRD patterns of MAPI and *d*-MAPI-PDA thin films along with aging up to 555 h. After 56 h, MAPI already started degrading as indicated by the small PbI_2 peak. The degradation started to be visible after around 297 h. After 456 h, the (001) PbI_2 peak was as intense as the (110) $MAPbI_3$ one. The film was finally totally degraded after 555 h, i.e., 23 days. During the whole aging process, no additional peaks were found, indicating an almost complete transformation of $MAPbI_3$ into PbI_2. In contrast, *d*-MAPI-PDA displayed a completely different degradation pathway. Indeed, after 56 h, the (001) PbI_2 peak (already present in the fresh film) did not see its intensity increase and the perovskite (110) peak intensity did not change either. However, the unknown phase-related peaks at 10.5 and 11.6°, observed in the fresh film, completely disappeared and another appeared at 10.3°. This shows that these unknown compounds present in the *d*-MAPI-PDA films are the first to be deteriorated after air exposure and not the perovskite. After 192 h, a slight increase of the PbI_2 was visible and two new peaks appeared at 8.5 and 10.6°. According to the literature, these peaks can be associated to the $MAPbI_3{\cdot}H_2O$ hydrate compound.[48] Hydration of *d*-MAPI-PDA occurs extremely slowly most probably because water molecules interact with PDA^{2+} cations which are present in the channels of the perovskite lattice.[34] On the other hand, for classic MAPI, hydration is quick.[48] After 339 h, the d-HP film degradation started to be slightly visible to the eye. After 480 h of aging, the intensity of $MAPbI_3{\cdot}H_2O$ peaks rose a second time, meaning severe hydration of the perovskite. New peaks at 10.1° and around 25° were observed. A possibility could have been the apparition of $MA_4PbI_6{\cdot}2H_2O$ but the 2θ values found in the literature did not match.[48] The phases responsible for these peaks remain to be clarified. It is also interesting to note how the intensity of the (110) peak of *d*-MAPI-PDA perovskite declines while the PbI_2 peak does not grow and the $MAPbI_3{\cdot}H_2O$ peaks do. These evolutions show the degradation pathway of the *d*-MAPI-PDA perovskite. Contrary to the classic MAPI that with humidity transforms very quickly into $MAPbI_3{\cdot}H_2O$ then rapidly into PbI_2, only a small amount of *d*-MAPI-PDA follows this degradation pathway. The majority of perovskite degrades into hydrated $MAPbI_3{\cdot}H_2O$ without transforming into PbI_2, thus trapping water inside the perovskite film. Overall, after 555 h, the intensities of the perovskite peaks are still quite high, and the film remains black while MAPI is almost entirely decomposed into PbI_2. The incorporation of PDA^{2+} cations within the perovskite lattice was proved to enhance considerably the stability of the MAPI perovskite by modifying integrally the degradation pathway of the perovskite.

We focused our further investigations on *d*-MAPI-PDA films and devices. Time-resolved photoluminescence (TRPL) measurements were performed on *d*-MAPI-PDA films deposited on FTO/c-TiO_2/m-TiO_2 substrates. The associated decay curves were fitted using a triple exponential function to obtain the best possible coefficient of determination R^2. The decay curves are depicted in Figure 4c,d. The triple exponential function used, and the extracted fitting parameters obtained are

https://doi.org/10.1021/acsomega.3c02292
ACS Omega 2023, 8, 23870−23879

Table 1. Average Photovoltaic $J-V$ Parameters with Standard Deviation of MAPI and *d*-MAPI-PDA PSCs

sample	scan direction	V_{OC} [V]	J_{SC} [mA.cm^{-2}]	FF [%]	PCE [%]	HI [%][a]
MAPI	reverse	1.05 ± 0.01	21.63 ± 0.44	79.41 ± 1.58	18.10 ± 0.54	16.2 ± 2.5
	forward	1.01 ± 0.02	21.65 ± 0.48	69.52 ± 1.17	15.16 ± 0.37	
d-MAPI-PDA	reverse	1.03 ± 0.02	19.23 ± 0.59	55.84 ± 2.36	11.07 ± 0.86	65.4 ± 6.1
	forward	0.81 ± 0.05	19.21 ± 0.61	24.45 ± 4.00	3.84 ± 0.79	

[a]Hysteresis index, noted HI, defined as $(PCE_{rev} - PCE_{fwd}) \times 100/PCE_{rev}$.

gathered in Table S6. By this fitting, two parameters τ_{fast} and τ_{slow} were determined. These parameters represent the nonradiative recombination at the electron transporting layer (ETL)/perovskite interface (reflecting the speed of charge injection in the transport layer) and the bimolecular recombination in the bulk of the perovskite (reflecting the bulk trap density), respectively. A higher τ_{slow} means much better bulk structural quality of the perovskite. A lower τ_{fast} value indicates better charge extraction at the ETL/perovskite layer, therefore, lower interface recombination centers and defect densities. *d*-MAPI-PDA exhibits a τ_{slow} value of 52.73 ns, 3.4 times higher than the τ_{slow} of 15.62 ns obtained from classic $MAPbI_3$. It indicates better bulk quality of the *d*-MAPI-PDA perovskite. This result is in agreement with the good crystallinity of *d*-MAPI-PDA observed by XRD (Figure 3b). The τ_{fast} values were measured at 0.72 ns for MAPI and 5.84 ns for *d*-MAPI-PDA, i.e., more than eight times the MAPI τ_{fast} value. It suggests a slower electron injection caused by a downgraded ETL/perovskite interface. We can note that poor charge injection leads to charge accumulation that can accentuate the hysteresis phenomenon. The improved bulk quality of the *d*-MAPI-PDA perovskite compared to $MAPbI_3$ may explain the better air stability observed for this d-HP perovskite.

Finally, we focused on the *d*-MAPI-PDA layer to investigate the potential application of the new d-HPs in complete operational perovskite solar cells (PSCs) with a FTO/c-TiO_2/m-TiO_2/perovskite/spiro-OMeTAD/Au architecture. $J-V$ curves of the best MAPI and *d*-MAPI-PDA cells are shown in Figure 5a, and the associated $J-V$ curve parameters are gathered in Table S7. The reference MAPI champion cell delivered a power conversion efficiency (PCE) of 18.48%, with a V_{OC} = 1.05 V, J_{SC} = 22.30 mA/cm^2, and FF = 79.13% measured on the reverse scan with a hysteresis index value of 15.8% (PCE = 15.6% in forward scan). On the other hand, the *d*-MAPI-PDA device reached the best efficiency of 13.00%, with a V_{OC} = 1.05 V, J_{SC} = 20.41 mA/cm^2, FF = 60.92%, and a hysteresis index (HI) = 63.8% (PCE = 4.70% in forward scan). Statistical $J-V$ parameter values of each system and their associated box charts are displayed in Table 1 and Figure S14, respectively. They confirm that the d-HP exhibits a very large HI. There have been many studies dedicated to the origin of the hysteresis loop on the $J-V$ curves of the perovskite solar cells. In the present case, our TRPL investigation has shown an unbalanced charge transport/extraction caused by the poor charge carrier extraction at the interface between the perovskite and the charge transport layer. If these parameters are not correctly paired, it causes a charge carrier accumulation near the ETL/perovskite (or perovskite/hole transporting layer (HTL)) interface. Ultimately, it will result in a capacitance phenomenon that produces hysteresis. The second origin that has been demonstrated in several studies, notably by Pauporté's and co-workers in refs 49, 50, is the ion migration, especially the migration of iodide. Ions can migrate under polarization and can accumulate near the charge transport layers, causing hysteresis under operation conditions. In the case of the d-HP, due to the special structure with the presence of PbI^+ lacunas, we suspect that iodide migration is favored. Moreover, the inserted PDA dication could be mobile, exacerbating the magnitude of hysteresis. The charge accumulation at the interface(s) and the nonoptimum charge transfer will exacerbate recombination and lower the current density and V_{OC} of *d*-MAPI-PDA solar cells, while the ionic migrations will reduce their fill factor.

After proving the feasibility of *d*-MAPI-PDA-based PSCs, we evaluated the stability of the PSCs. The cells were kept in air under the same conditions as the films to have a valid comparison (RH = 70−90%, $T°$ = 16−18 °C). The evolution of the cell normalized PCE as a function of aging time is depicted in Figure 5b. For the first fifty hours, the devices exhibited the same decrease in efficiency. After 50 h, the MAPI cell efficiency continued to decrease rapidly. It retained around 40% of its original PCE after 150 h of aging. From this point onward, the efficiency kept decreasing steadily but at a much slower pace to finally reach 26% of its original PCE after 464 h. Contrarily, after 50 h, the *d*-MAPI-PDA device exhibited a plateau for 200 h, during which the device retained 60% of its original PCE. After 270 h, the plateau ceased and the efficiency decreased once more, at a steady pace, to finally retain 40% of the initial PCE. Whether in films or in complete PSCs, the *d*-MAPI-PDA perovskite exhibited superior stability compared to its classic $MAPbI_3$ counterpart.

CONCLUSIONS

We have reported the successful incorporation of the big organic dication PDA^{2+} into 3D $MAPbI_3$ and $FAPbI_3$ perovskite lattice, thus creating new 3D d-HPs bypassing the tolerance factor. Such perovskites were notably synthesized as crystals and powders and characterized, for various amounts of PDA^{2+} cations: *d*-MAPI-$PDA_{0.05}$, *d*-MAPI-$PDA_{0.07}$, *d*-MAPI-$PDA_{0.08}$, *d*-α-FAPI-$PDA_{0.02}$, *d*-α-FAPI-$PDA_{0.04}$, and *d*-α-FAPI-$PDA_{0.07}$. A noteworthy point is the room temperature synthesis of pure α-FAPI perovskite-type (as *d*-α-FAPI-PDA_x) powders as well as the thin film preparation at a temperature of 125 °C, well-below the commonly used 150 °C. After a thorough analysis, general formulations of $(PDA)_{0,88x}(MA)_{1-0,76x}[Pb_{1-x}I_{3-x}]$ for *d*-MAPI-PDA and $(PDA)_{1,11x}(FA)_{1-1,22x}[Pb_{1-x}I_{3-x}]$ for *d*-α-FAPI-PDA were proposed.

Thin films of 3D *d*-MAPI-PDA_x and *d*-FAPI-PDA_x were also obtained for two different x values: *d*-MAPI-$PDA_{0.06}$, *d*-MAPI-$PDA_{0.08}$, *d*-FAPI-$PDA_{0.05}$, and *d*-FAPI-$PDA_{0.07}$. A high crystallinity of the films as well as certain scalability of the band gap was observed, depending on the amount of PDA^{2+} cations. These films exhibited excellent stability once stored in air, far surpassing the one of the classic $MAPbI_3$ and $FAPbI_3$. TRPL measurements conducted on *d*-MAPI-PDA demonstrated superior bulk quality of the perovskite after PDA^{2+}

https://doi.org/10.1021/acsomega.3c02292
ACS Omega 2023, 8, 23870−23879

incorporation, explaining such an impressive stability under ambient conditions. Finally, *d*-MAPI-PDA films were tested in PSCs and delivered a champion efficiency of 13.0% with good reproducibility and stability, proving the feasibility of *d*-MAPI-PDA PSCs.

EXPERIMENTAL SECTION

The thin film preparation methods, the PSC preparation methods, and the PSC characterization methods are provided in the Supporting Information.

Synthesis of Crystals and Powders. *Iodide Salt of Dication (PDAI$_2$, IH$_3$N−CH$_2$−CH(OH)−CH$_2$−NH$_3$I).* Crystals of PDAI$_2$ were obtained by solvent evaporation. One molar equivalent of 1,3-diaminopropan-2-ol (H$_2$N−CH$_2$−CH(OH)−CH$_2$−NH$_2$, Combi-Blocks, 98%) was added and dissolved into 2.4 molar equivalents of an aqueous solution of hydroiodic acid (HI$_{(aq)}$, Alfa Aesar, 57 wt %) at room temperature. Then, this aqueous solution was placed under a gaseous stream of nitrogen leading to a complete evaporation of water together with the formation of white/colorless PDAI$_2$ crystals. The PDAI$_2$ crystals were washed several times by ethyl acetate (Carlo Erba Reagents) and then stocked into a desiccator.

Crystals of d-MAPI-PDA$_x$. Crystals of *d*-MAPI-**PDA$_x$** were obtained by the inverse temperature crystallization (ITC) method. First, the precursors PDAI$_2$, methylammonium iodide (MAI, Greatcell Solar Materials), and lead iodide (PbI$_2$, Sigma Aldrich, 99%) were dissolved into γ-butyrolactone (GBL) under agitation at 60 °C, exhibiting a PbI$_2$ concentration of 1.0 mol L^{-1} and the stoichiometries 1−1.25/3/3 (PDAI$_2$/MAI/PbI$_2$, respectively). Second, the precursor solution was heated to 100 °C for 30 min, leading to black *d*-MAPI-PDA$_x$ crystals. Finally, the crystals were filtered, dried, and stored in a desiccator.

Powders of d-MAPI-PDA$_x$ and MAPI. MAPI and three compositions of *d*-MAPI-**PDA$_x$** powders were obtained (*d*-MAPI-**PDA$_{0.05}$** with x = 0.05, *d*-MAPI-**PDA$_{0.07}$** with x = 0.07, and *d*-MAPI-**PDA$_{0.08}$** with x = 0.08), all by the fast precipitation method, at room temperature. The precursors PDAI$_2$, MAI, and PbI$_2$ were dissolved into 0.5 mL of GBL (at 60 °C), with a PbI$_2$ concentration of 1.0 mol L^{-1} and respecting the accurate stoichiometries 0.10/3/3 (PDAI$_2$/MAI/PbI$_2$, respectively) for *d*-MAPI-**PDA$_{0.05}$**, 0.15/3/3 for *d*-MAPI-**PDA$_{0.07}$**, 0.20/3/3 for *d*-MAPI-**PDA$_{0.08}$**, and 0/3/3 for MAPI. Then, precursor solutions were separately added into 2 mL of ethyl acetate previously heated to 60 °C, immediately leading to the precipitation of the *d*-MAPI-**PDA$_{0.05}$**, *d*-MAPI-**PDA$_{0.07}$**, *d*-MAPI-**PDA$_{0.08}$**, and MAPI black powders. These precipitated powders were filtered, several times washed with ethyl acetate, dried, and stored in a desiccator.

Powders of d-α-FAPI-PDA$_x$ and α-FAPI. α-FAPI and three compositions of *d*-α-FAPI-**PDA$_x$** powders were obtained (*d*-FAPI-**PDA$_{0.02}$** with x = 0.02, *d*-FAPI-**PDA$_{0.04}$** with x = 0.04, and *d*-FAPI-**PDA$_{0.07}$** with x = 0.07), all by the same fast precipitation method employed for *d*-MAPI-**PDA$_x$** powders. The precursors PDAI$_2$, FAI, and PbI$_2$ were dissolved into 0.5 mL of GBL (at 60 °C), with a PbI$_2$ concentration of 1.0 mol L^{-1} and respecting the accurate stoichiometries 0.15/3/3 (PDAI$_2$/FAI/PbI$_2$, respectively) for *d*-FAPI-**PDA$_{0.02}$**, 0.20/3/3 for *d*-FAPI-**PDA$_{0.04}$**, 0.25/3/3 for *d*-FAPI-**PDA$_{0.07}$**, and 0/3/3 for α-FAPI. Then, this precursor solutions were each separately added into 2 mL of ethyl acetate (which has been previously heated to 60 °C), immediately leading to precipitation of *d*-FAPI-**PDA$_{0.02}$**, *d*-FAPI-**PDA$_{0.04}$**, and *d*-FAPI-**PDA$_{0.07}$** black powders. Concerning α-FAPI, the obtained precipitate powder was the yellow δ-FAPI phase, and it is only after the subsequent heating at 155 °C that the black α-FAPI was formed. All these precipitated powders were filtered, washed several times with ethyl acetate, dried in an oven (at 155 °C for the reference α-FAPI, below 100 °C for *d*-FAPI-**PDA$_{0.02}$**, *d*-FAPI-**PDA$_{0.04}$**, and *d*-FAPI-**PDA$_{0.07}$**), and then stored in a desiccator.

Characterization of Crystals, Powders, and Thin Films. Single crystal XRD data collection was performed using an Agilent supernova diffractometer (copper radiation source, λ_{Cu} = 154,184 Å). Powder and thin film XRD data collection was carried out using a D8 Bruker diffractometer (copper radiation source), equipped with a scintillation detector. EDX-MEB measurements were performed with a Zeiss EVO LS10. Carbon coating (3 nm) deposition was realized for all powder samples. Employed calibrations: Intensity = 200 pA/EHT = 20 kV/Diaphragm: 30 μm. ^{1}H NMR (solution) spectra (300 MHz) were recorded with a Bruker ultrashield TM 300 MHz spectrometer (magnetic field 7 T) using deuterated dimethylsulfoxide (*DMSO-d$_6$*) as the solvent. ^{13}C solid-state NMR spectra were acquired with a Bruker Avance III 300 MHz spectrometer (magnetic field 7 T) equipped with a 4 mm H/X dual probe under magic angle spinning with 5 kHz. For 2 ms contact time cross-polarization (CP) spectra, 2 K scans were accumulated with a recycle delay of 5 s, for direct excitation spectra 1−2.5 K scans with a recycle delay of 40 s by means of the DEPTH sequence for suppression of background signals. C, H, N, and O elemental analyses were measured with a Flash 2000 Organic Elemental Analyzer, while elemental analysis of lead was realized by the microanalysis method at the Crealins company (Villeurbanne, France).

ASSOCIATED CONTENT

Supporting Information

The Supporting Information is available free of charge at https://pubs.acs.org/doi/10.1021/acsomega.3c02292.

PXRD; ^{1}H NMR (solution); ^{13}C solid-state NMR; elemental analysis; thin film preparation; SEM; and solar cell characteristics (PDF)

AUTHOR INFORMATION

Corresponding Authors

Nicolas Mercier − *University of Angers, MOLTECH-Anjou, UMR 6200, 49045 Angers, France;* orcid.org/0000-0003-0458-0789; Email: nicolas.mercier@univ-angers.fr

Thierry Pauporté − *Chimie-ParisTech, PSL Université, CNRS, Institut de Recherche de Chimie-Paris (IRCP), UMR8247, F-75231 cedex 05 Paris, France;* Email: thierry.pauporte@chimieparistech.fr

Authors

Liam Gollino − *Chimie-ParisTech, PSL Université, CNRS, Institut de Recherche de Chimie-Paris (IRCP), UMR8247, F-75231 cedex 05 Paris, France*

Antonin Leblanc − *University of Angers, MOLTECH-Anjou, UMR 6200, 49045 Angers, France*

Jens Dittmer − *Le Mans Université, Institut des Molécules et Matériaux du Mans (IMMM), CNRS UMR 6283, 72085 cedex 9 Le Mans, France*

https://doi.org/10.1021/acsomega.3c02292
ACS Omega 2023, 8, 23870−23879

Complete contact information is available at:
https://pubs.acs.org/10.1021/acsomega.3c02292

Notes

The authors declare no competing financial interest.

■ ACKNOWLEDGMENTS

The Agence Nationale de la Recherche is acknowledged for financial support via the Moreless project ANR-18-CE05-00026.

■ REFERENCES

(1) Lee, M. M.; Teuscher, J.; Miyasaka, T.; Murakami, T. N.; Snaith, H. J. Efficient Hybrid Solar Cells Based on Meso-Superstructured Organometal Halide Perovskites. *Science* **2012**, *338*, 643−647.
(2) Chung, I.; Lee, B.; He, J.; Chang, R. P. H.; Kanatzidis, M. G. All-Solid-State Dye-Sensitized Solar Cells with High Efficiency. *Nature* **2012**, *485*, 486−489.
(3) Kim, H.-S.; Lee, C.-R.; Im, J.-H.; Lee, K.-B.; Moehl, T.; Marchioro, A.; Moon, S.-J.; Humphry-Baker, R.; Yum, J.-H.; Moser, J. E.; Grätzel, M.; Park, N.-G. Lead Iodide Perovskite Sensitized All-Solid-State Submicron Thin Film Mesoscopic Solar Cell with Efficiency Exceeding 9%. *Sci. Rep.* **2012**, *2*, 591.
(4) Chen, Z.; Wang, J. J.; Ren, Y.; Yu, C.; Shum, K. Schottky Solar Cells Based on CsSnI 3 Thin-Films. *Appl. Phys. Lett.* **2012**, *101*, No. 093901.
(5) Yin, W.-J.; Shi, T.; Yan, Y. Unique Properties of Halide Perovskites as Possible Origins of the Superior Solar Cell Performance. *Adv. Mater.* **2014**, *26*, 4653−4658.
(6) Stoumpos, C. C.; Malliakas, C. D.; Kanatzidis, M. G. Semiconducting Tin and Lead Iodide Perovskites with Organic Cations: Phase Transitions, High Mobilities, and Near-Infrared Photoluminescent Properties. *Inorg. Chem.* **2013**, *52*, 9019−9038.
(7) Stranks, S. D.; Eperon, G. E.; Grancini, G.; Menelaou, C.; Alcocer, M. J. P.; Leijtens, T.; Herz, L. M.; Petrozza, A.; Snaith, H. J. Electron-Hole Diffusion Lengths Exceeding 1 Micrometer in an Organometal Trihalide Perovskite Absorber. *Science* **2013**, *342*, 341−344.
(8) Luo, D.; Su, R.; Zhang, W.; Gong, Q.; Zhu, R. Minimizing Non-Radiative Recombination Losses in Perovskite Solar Cells. *Nat. Rev. Mater.* **2020**, *5*, 44−60.
(9) Sutton, R. J.; Eperon, G. E.; Miranda, L.; Parrott, E. S.; Kamino, B. A.; Patel, J. B.; Hörantner, M. T.; Johnston, M. B.; Haghighirad, A. A.; Moore, D. T.; Snaith, H. J. Bandgap-Tunable Cesium Lead Halide Perovskites with High Thermal Stability for Efficient Solar Cells. *Adv. Energy Mater.* **2016**, *6*, No. 1502458.
(10) Leyden, M. R.; Terakawa, S.; Matsushima, T.; Ruan, S.; Goushi, K.; Auffray, M.; Sandanayaka, A. S. D.; Qin, C.; Bencheikh, F.; Adachi, C. Distributed Feedback Lasers and Light-Emitting Diodes Using 1-Naphthylmethylamnonium Low-Dimensional Perovskite. *ACS Photonics* **2019**, *6*, 460−466.
(11) Wei, Y.; Cheng, Z.; Lin, J. An Overview on Enhancing the Stability of Lead Halide Perovskite Quantum Dots and Their Applications in Phosphor-Converted LEDs. *Chem. Soc. Rev.* **2019**, *48*, 310−350.
(12) Miao, J.; Zhang, F. Recent Progress on Highly Sensitive Perovskite Photodetectors. *J. Mater. Chem. C* **2019**, *7*, 1741−1791.
(13) Wang, H.; Kim, D. H. Perovskite-Based Photodetectors: Materials and Devices. *Chem. Soc. Rev.* **2017**, *46*, 5204−5236.
(14) Mykhaylyk, V. B.; Kraus, H.; Saliba, M. Bright and Fast Scintillation of Organolead Perovskite MAPbBr3 at Low Temperatures. *Mater. Horizons* **2019**, *6*, 1740−1747.
(15) Yang, M.; Zhang, T.; Schulz, P.; Li, Z.; Li, G.; Kim, D. H.; Guo, N.; Berry, J. J.; Zhu, K.; Zhao, Y. Facile Fabrication of Large-Grain CH3NH3PbI3−xBrx Films for High-Efficiency Solar Cells via CH3NH3Br-Selective Ostwald Ripening. *Nat. Commun.* **2016**, *7*, 12305.
(16) Saliba, M.; Matsui, T.; Domanski, K.; Seo, J.-Y.; Ummadisingu, A.; Zakeeruddin, S. M.; Correa-Baena, J.-P.; Tress, W. R.; Abate, A.; Hagfeldt, A.; Grätzel, M. Incorporation of Rubidium Cations into Perovskite Solar Cells Improves Photovoltaic Performance. *Science* **2016**, *354*, 206−209.
(17) Saliba, M.; Matsui, T.; Seo, J.-Y.; Domanski, K.; Correa-Baena, J.-P.; Nazeeruddin, M. K.; Zakeeruddin, S. M.; Tress, W.; Abate, A.; Hagfeldt, A.; Grätzel, M. Cesium-Containing Triple Cation Perovskite Solar Cells: Improved Stability, Reproducibility and High Efficiency. *Energy Environ. Sci.* **2016**, *9*, 1989−1997.
(18) Turren-Cruz, S.-H.; Hagfeldt, A.; Saliba, M. Methylammonium-Free, High-Performance, and Stable Perovskite Solar Cells on a Planar Architecture. *Science* **2018**, *362*, 449−453.
(19) Toscano, C. D.; Guilarte, T. R. Lead Neurotoxicity: From Exposure to Molecular Effects. *Brain Res. Rev.* **2005**, *49*, 529−554.
(20) Jaishankar, M.; Tseten, T.; Anbalagan, N.; Mathew, B. B.; Beeregowda, K. N. Toxicity, Mechanism and Health Effects of Some Heavy Metals. *Interdiscip. Toxicol.* **2014**, *7*, 60−72.
(21) Benmessaoud, I. R.; Mahul-Mellier, A.-L.; Horváth, E.; Maco, B.; Spina, M.; Lashuel, H. A.; Forró, L. Health Hazards of Methylammonium Lead Iodide Based Perovskites: Cytotoxicity Studies. *Toxicol. Res.* **2016**, *5*, 407−419.
(22) Finkelstein, Y.; Markowitz, M. E.; Rosen, J. F. Low-Level Lead-Induced Neurotoxicity in Children: An Update on Central Nervous System Effects. *Brain Res. Rev.* **1998**, *27*, 168−176.
(23) Abate, A. Perovskite Solar Cells Go Lead Free. *Joule* **2017**, *1*, 659−664.
(24) Nie, R.; Sumukam, R. R.; Reddy, S. H.; Banavoth, M.; Seok, S. I. Lead-Free Perovskite Solar Cells Enabled by Hetero-Valent Substitutes. *Energy Environ. Sci.* **2020**, *13*, 2363−2385.
(25) Xiao, Z.; Song, Z.; Yan, Y. From Lead Halide Perovskites to Lead-Free Metal Halide Perovskites and Perovskite Derivatives. *Adv. Mater.* **2019**, *31*, No. 1803792.
(26) Gu, S.; Lin, R.; Han, Q.; Gao, Y.; Tan, H.; Zhu, J. Tin and Mixed Lead−Tin Halide Perovskite Solar Cells: Progress and Their Application in Tandem Solar Cells. *Adv. Mater.* **2020**, *32*, No. 1907392.
(27) Kour, R.; Arya, S.; Verma, S.; Gupta, J.; Bandhoria, P.; Bharti, V.; Datt, R.; Gupta, V. Potential Substitutes for Replacement of Lead in Perovskite Solar Cells: A Review. *Global Chall.* **2019**, *3*, No. 1900050.
(28) Gollino, L.; Pauporté, T. Lead-Less Halide Perovskite Solar Cells. *Sol. RRL* **2021**, *5*, No. 2000616.
(29) Nielsen, P. K.; Hemmingsen, C.; Friis, S. U.; Ladefoged, J.; Olgaard, K. Comparison of Straight and Curled Tenckhoff Peritoneal Dialysis Catheters Implanted by Percutaneous Technique: A Prospective Randomized Study. *Perit. Dial. Int. J. Int. Soc. Perit. Dial.* **1995**, *15*, 18−21.
(30) Bartel, C. J.; Sutton, C.; Goldsmith, B. R.; Ouyang, R.; Musgrave, C. B.; Ghiringhelli, L. M.; Scheffler, M. New Tolerance Factor to Predict the Stability of Perovskite Oxides and Halides. *Sci. Adv.* **2019**, *5*, No. eaav0693.
(31) Zhu, T.; Su, J.; Labat, F.; Ciofini, I.; Pauporté, T. Interfacial Engineering through Chloride-Functionalized Self-Assembled Monolayers for High-Performance Perovskite Solar Cells. *ACS Appl. Mater. Interfaces* **2020**, *12*, 744−752.
(32) Zheng, D.; Zhu, T.; Yan, Y.; Pauporté, T. Controlling the Formation Process of Methylammonium-Free Halide Perovskite Films for a Homogeneous Incorporation of Alkali Metal Cations Beneficial to Solar Cell Performance. *Adv. Energy Mater.* **2022**, *12*, No. 2103618.
(33) Zheng, D.; Chen, F.; Rager, M.; Gollino, L.; Zhang, B.; Pauporté, T. What Are Methylammonium and Solvent Fates upon Halide Perovskite Thin-Film Preparation and Thermal Aging? *Adv. Mater. Interfaces* **2022**, *9*, No. 2201436.
(34) Leblanc, A.; Mercier, N.; Allain, M.; Dittmer, J.; Fernandez, V.; Pauporté, T. Lead- and Iodide-Deficient (CH 3 NH 3)PbI 3 (d -MAPI): The Bridge between 2D and 3D Hybrid Perovskites. *Angew. Chem. Int. Ed.* **2017**, *56*, 16067−16072.

(35) Leblanc, A.; Mercier, N.; Allain, M.; Dittmer, J.; Pauporté, T.; Fernandez, V.; Boucher, F.; Kepenekian, M.; Katan, C. Enhanced Stability and Band Gap Tuning of α-[HC(NH 2) 2]PbI 3 Hybrid Perovskite by Large Cation Integration. *ACS Appl. Mater. Interfaces* **2019**, *11*, 20743−20751.
(36) Jayanthi, K.; Spanopoulos, I.; Zibouche, N.; Voskanyan, A. A.; Vasileiadou, E. S.; Islam, M. S.; Navrotsky, A.; Kanatzidis, M. G. Entropy Stabilization Effects and Ion Migration in 3D "Hollow" Halide Perovskites. *J. Am. Chem. Soc.* **2022**, *144*, 8223−8230.
(37) Spanopoulos, I.; Hadar, I.; Ke, W.; Guo, P.; Mozur, E. M.; Morgan, E.; Wang, S.; Zheng, D.; Padgaonkar, S.; Manjunatha Reddy, G. N.; Weiss, E. A.; Hersam, M. C.; Seshadri, R.; Schaller, R. D.; Kanatzidis, M. G. Tunable Broad Light Emission from 3D "Hollow" Bromide Perovskites through Defect Engineering. *J. Am. Chem. Soc.* **2021**, *143*, 7069−7080.
(38) Ke, W.; Spanopoulos, I.; Tu, Q.; Hadar, I.; Li, X.; Shekhawat, G. S.; Dravid, V. P.; Kanatzidis, M. G. Ethylenediammonium-Based "Hollow" Pb/Sn Perovskites with Ideal Band Gap Yield Solar Cells with Higher Efficiency and Stability. *J. Am. Chem. Soc.* **2019**, *141*, 8627−8637.
(39) Senocrate, A.; Spanopoulos, I.; Zibouche, N.; Maier, J.; Islam, M. S.; Kanatzidis, M. G. Tuning Ionic and Electronic Conductivities in the "Hollow" Perovskite {En}MAPbI3. *Chem. Mater.* **2021**, *33*, 719−726.
(40) Ke, W.; Stoumpos, C. C.; Spanopoulos, I.; Mao, L.; Chen, M.; Wasielewski, M. R.; Kanatzidis, M. G. Efficient Lead-Free Solar Cells Based on Hollow {en}MASnI 3 Perovskites. *J. Am. Chem. Soc.* **2017**, *139*, 14800−14806.
(41) Spanopoulos, I.; Ke, W.; Stoumpos, C. C.; Schueller, E. C.; Kontsevoi, O. Y.; Seshadri, R.; Kanatzidis, M. G. Unraveling the Chemical Nature of the 3D "Hollow" Hybrid Halide Perovskites. *J. Am. Chem. Soc.* **2018**, *140*, 5728−5742.
(42) Ke, W.; Stoumpos, C. C.; Zhu, M.; Mao, L.; Spanopoulos, I.; Liu, J.; Kontsevoi, O. Y.; Chen, M.; Sarma, D.; Zhang, Y.; Wasielewski, M. R.; Kanatzidis, M. G. Enhanced Photovoltaic Performance and Stability with a New Type of Hollow 3D Perovskite {en}FASnI 3. *Sci. Adv.* **2017**, *3*, No. e1701293.
(43) Ke, W.; Stoumpos, C. C.; Spanopoulos, I.; Chen, M.; Wasielewski, M. R.; Kanatzidis, M. G. Diammonium Cations in the FASnI 3 Perovskite Structure Lead to Lower Dark Currents and More Efficient Solar Cells. *ACS Energy Lett.* **2018**, *3*, 1470−1476.
(44) Lu, D.; Lv, G.; Xu, Z.; Dong, Y.; Ji, X.; Liu, Y. Thiophene-Based Two-Dimensional Dion−Jacobson Perovskite Solar Cells with over 15% Efficiency. *J. Am. Chem. Soc.* **2020**, *142*, 11114−11122.
(45) Fu, P.; Liu, Y.; Yu, S.; Yin, H.; Yang, B.; Ahmad, S.; Guo, X.; Li, C. Dion-Jacobson and Ruddlesden-Popper Double-Phase 2D Perovskites for Solar Cells. *Nano Energy* **2021**, *88*, No. 106249.
(46) Cohen, B.-E.; Binyamin, T.; Ben-Tzvi, T.; Goldberg, O.; Schlesinger, A.; Balberg, I.; Millo, O.; Gross, E.; Azulay, D.; Etgar, L. Hydroxyl Functional Groups in Two-Dimensional Dion−Jacobson Perovskite Solar Cells. *ACS Energy Lett.* **2022**, *7*, 217−225.
(47) Chen, Y.; Hu, J.; Xu, Z.; Jiang, Z.; Chen, S.; Xu, B.; Xiao, X.; Liu, X.; Forberich, K.; Brabec, C. J.; Mai, Y.; Guo, F. Managing Phase Orientation and Crystallinity of Printed Dion−Jacobson 2D Perovskite Layers via Controlling Crystallization Kinetic. *Adv. Funct. Mater.* **2022**, *32*, No. 2112146.
(48) Leguy, A. M. A.; Hu, Y.; Campoy-Quiles, M.; Alonso, M. I.; Weber, O. J.; Azarhoosh, P.; van Schilfgaarde, M.; Weller, M. T.; Bein, T.; Nelson, J.; Docampo, P.; Barnes, P. R. F. Reversible Hydration of CH 3 NH 3 PbI 3 in Films, Single Crystals, and Solar Cells. *Chem. Mater.* **2015**, *27*, 3397−3407.
(49) Zheng, D.; Zhu, T.; Pauporté, T. A Co-Additives Strategy for Blocking Ionic Mobility in Methylammonium-Free Perovskite Solar Cells and High Stability Achievement. *Solar RRL.* **2021**, *5*, No. 2100010.
(50) Zheng, D.; Raffin, F.; Volovitch, P.; Pauporté, T. Control of perovskite film crystallization and growth direction to target homogeneous. monolithic structures. *Nat. Commun.* **2022**, *13*, 6655.

https://doi.org/10.1021/acsomega.3c02292
ACS Omega 2023, 8, 23870−23879